Iris Recognition: On the Segmentation of Degraded Images Acquired in the Visible Wavelength

Hugo Proença

Abstract—Iris recognition imaging constraints are receiving increasing attention. There are several proposals to develop systems that operate in the visible wavelength and in less constrained environments. These imaging conditions engender acquired noisy artifacts that lead to severely degraded images, making iris segmentation a major issue. Having observed that existing iris segmentation methods tend to fail in these challenging conditions, we present a segmentation method that can handle degraded images acquired in less constrained conditions. We offer the following contributions: 1) to consider the sclera the most easily distinguishable part of the eye in degraded images, 2) to propose a new type of feature that measures the proportion of sclera in each direction and is fundamental in segmenting the iris, and 3) to run the entire procedure in deterministically linear time in respect to the size of the image, making the procedure suitable for real-time applications.

Index Terms—Iris segmentation, biometrics, noncooperative image acquisition, visible-light iris images, covert recognition.

✦

1 INTRODUCTION

THE human iris supports contactless data acquisition and can be imaged covertly. Thus, at least theoretically, the subsequent biometric recognition procedure can be performed without subjects' knowledge. The feasibility of this type of recognition has received increasing attention and is of particular interest for forensic and security purposes, such as the pursuit of criminals and terrorists and the search for missing children.

Deployed iris recognition systems are mainly based on Daugman's pioneering approach, and have proven their effectiveness in relatively constrained scenarios: operating in the near-infrared spectrum (NIR, 700-900 nm), at close acquisition distances and with stop-and-stare interfaces. These systems require high illumination levels, sufficient to maximize the signal-to-noise ratio in the sensor and to capture images of the discriminating iris features with sufficient contrast. However, if similar processes were used to acquire iris images from a distance, acceptable depth-of-field values would demand significantly higher f-numbers for the optical system, corresponding directly (squared) with the amount of light required for the process. Similarly, the motion factor will demand very short exposure times, which again will require too high levels of light. The American and European standards councils ([1] and [8]) proposed safe irradiance limits for NIR illumination of near $10 \, \mathrm{mW/cm^2}$. In addition to other factors that determine

imaging system safety (blue light, nonreciprocity, and wavelength dependence), these limits should be taken into account, as excessively strong illumination can cause permanent eye damage. The NIR wavelength is particularly hazardous because the eye does not instinctively respond with its natural mechanisms (aversion, blinking, and pupil contraction). However, the use of visible light and unconstrained imaging setups can severely degrade the quality of the captured data (Fig. 1), increasing the challenges in performing reliable recognition.

The pigmentation of the human iris consists mainly of two molecules: brown-black Eumelanin (over 90 percent) and yellow-reddish Pheomelanin [26]. Eumelanin has most of its radiative fluorescence under the VW, which—if properly imaged—enables the capture of a much higher level of detail, but also of many more noisy artifacts, including specular and diffuse reflections and shadows. Also, the spectral reflectance of the sclera is significantly higher in the VW than in the NIR (Fig. 2a) and the spectral radiance of the iris in respect of the levels of its pigmentation varies much more significantly in the VW than in the NIR (Fig. 2b). All of these observations justify the need for specialized segmentation strategies, as the type of imaged information is evidently different. Furthermore, traditional template and boundary-based iris segmentation approaches will probably fail, due to difficulties in detecting edges or in fitting rigid shapes. These observations were the major motivation behind the work described in this paper: the development of an iris segmentation technique designed specifically for degraded iris images acquired in the VW and unconstrained scenarios.

First, we describe a deterministic linear-time algorithm to discriminate nonparametrically between noise-free iris pixels and all other types of data. The key insights behind our algorithm are: 1) to consider the sclera as the most easily detectable part of the eye in degraded VW images, and 2) that

● *The author is with the Departameto de Informética, Universidade da Beira Interior, Rua Marqus D'Avila e Bolama, 6201-001 Covilhã, Portugal. E-mail: hugomcp@di.ubi.pt.*

Fig. 1. Comparison between (a) the quality of iris biometric images acquired in highly constrained conditions in the near-infrared wavelength (WVU database [39]) and (b) images acquired in the visible wavelength in unconstrained imaging conditions, acquired at-a-distance and on-the-move (UBIRIS.v2 database [38]).

invariably, the sclera is contiguous and surrounds the iris region, which is used in the detection and segmentation of the iris. The algorithm is based on the neural pattern recognition paradigm. Its spatial and temporal complexity is deterministic and classified as linear time (O(n)), as its asymptotic upper bound is linearly proportional to the size of the input data (n). We also present a method for parameterizing segmented data because this parameterization is required for subsequent processing. We frame this task as a constrained least squares minimization in order to compute the polynomial regression of two functions that approximate the iris inner and outer borders. We justify the use of this technique by its ability to parameterize data with arbitrary order while smoothing its shape and compensating for small inaccuracies from the previous classification stage.

The remainder of this paper is organized as follows: Section 2 briefly summarizes the most popular iris segmentation methods, emphasizing those most recently published. In Section 3, we describe our method in detail. Section 4 describes our experiments and discusses our results. Finally, Section 5 concludes.

2   IRIS RECOGNITION

This section summarizes several recently published works about iris imaging constraints and acquisition protocols. Later, within the scope of this paper, we analyze and compare several iris segmentation proposals, especially focusing on those that may be more robust against degraded data.

2.1   Less Constrained Image Capturing

The "Iris-on-the-move" project [25] should be emphasized: It is a major example of engineering an image acquisition system to make the recognition process less intrusive for subjects. The goal is to acquire NIR close-up iris images as a subject walks at normal speed through an access control point. *Honeywell Technologies* applied for a patent [19] on a very similar system, which was also able to recognize irises at-a-distance. Previously, Fancourt et al. [13] concluded that it is possible to acquire sufficiently high-quality images at a distance of up to 10 meters. Narayanswamy et al. [29] used a wave-front coded optic to deliberately blur images in such a way that they do not change over a large depth-of-field. Removing the blur with digital image processing techniques makes the trade-off between signal-to-noise ratio and depth-of-field linear. Also, using wave-front coding technology, Smith et al. [42] examined the iris information that could be captured in the NIR and VW spectra, addressing the possibility of using these multispectral data to improve recognition performance. Park and Kim [32] acquired in-focus iris images quickly at-a-distance, and Boddeti and Kumar [5] suggested extending the depth-of-field of iris imaging frameworks by using correlation filters. He et al. [17] analyzed the role of different NIR wavelengths in determining error rates. More recently, Yoon et al. [47] presented an imaging framework that can acquire NIR iris images at-a-distance of up to 3 meters, based on a face detection module and on a light-stripe laser device used to point the camera at the proper scene region. Boyce et al. [6]
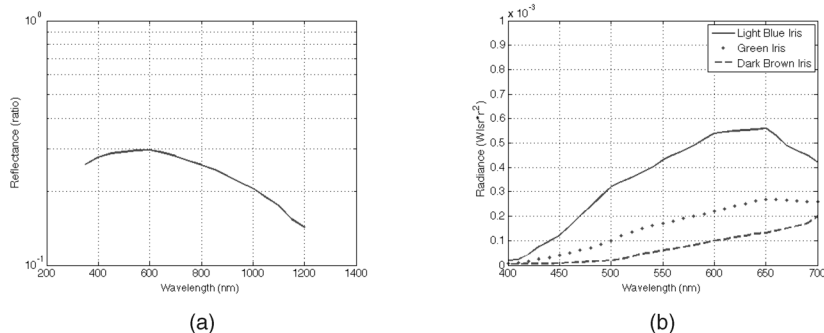
Fig. 2. Spectral reflectance and radiance of the iris and the sclera in respect of the wavelength. (a) Spectral reflectance of the human sclera [31]. (b) Spectral radiance of the human iris according to the levels of iris pigmentation [21].

TABLE 1
Overview of the Most Relevant Recently Published Iris Segmentation Methods

Method	Experiments	Preprocessing	Ord. Borders	Pupillary Border	Scleric Border
Zuo et al. [50]	CASIA.1, ICE, WVU (NIR)	Specular reflections detected (threshold), PDE and impainting	P → S	Randomized Elliptical Hough Transform	Weighted Integro-differential operator
Puhan et al. [28]	UBIRIS (VW)	Image binarization (threshold of the local Fourier spectral density)	S	-	Construction of a set of unidimensional signals, gradient analysis
Ross and Shah [40]	CASIA.1, WVU (NIR)	2-D Median filter	P → S	Binarization (threshold), Circular Hough Transform	Geodesic Active Contours
Poursaberi and Araabi [35]	CASIA.1 (NIR)	Negative image, impainting	P	Iterative expansion/shrink of the detected border based on morphological operators	-
Morimoto et al. [27]	Non-specified (NIR)	Not described	P → S	Images difference	Images cascade at different scales, Sobel edges detection, elliptical form fitting
Liu et al. [23]	ICE (NIR)	Not described	P → S	Angular constrained Canny edge detection, Hough-based transform	Hough-based form fitting, hypothesis and test process
Kennell et al. [22]	BATH (NIR)	Histogram equalization, image binarization (threshold)	P → S	Morphological operators, integro-differential operator	Image binarization based on pixels+ neighborhood variance, form fitting
Vatsa et al. [44]	UBIRIS, CASIA.v3 (NIR, VW)	Not described	P → S	Rough estimation according to an elliptical model, followed by a modified Mumford-Shah functional	Process similar to the pupillary border
Proença and Alexandre [37]	UBIRIS (VW)	Histogram equalization	S → P	Feature extraction (pixel position + intensity) and fuzzy clustering to reduce image heterogeneity, Canny edges detection and circular Hough transform	Process similar to the pupillary border
Zaim [48]	CASIA.1 (NIR)	Morphologic operators to eliminate eyelashes	S → P	Split and merge process to localize regions of uniform intensity	Image normalization based on pupil coordinates, Sobel filtering, detection of horizontal edges in the normalized image
Broussard et al. [7]	BATH (NIR)	Not described	P,S	Extraction of local texture features, feed forward neural network	Process similar to the pupillary border
He and Shi [16]	Non-specified (NIR)	Image binarization, morphologic operations	P → S	Geometrical projection methods, Sobel filtering, form fitting	Canny edge extraction, Hough transform
Basit and Javed [3]	BATH (NIR)	Image binarization, morphologic operations	P → S	Iterative bijections-based method	Maximization of the difference of intensities of radial direction
Arvacheh and Tizhoosh [2]	CASIA.1 (NIR)	Not described	P → S	Near circular active contour model (snakes), interpolation process to improve performance	Integro-differential operator
Daugman [10]	ICE (NIR)	Not described	P → S	Active contours based on Fourier series, modeled with 17 discrete Fourier coefficients	Active contours based on Fourier series, modeled with 4 discrete Fourier coefficients
He et al. [18]	CASIA.1 (NIR)	Not described	P → S	Adaboost based object detection, iterative circumference shifting	Image normalization, Sobel and Canny filtering, line fitting
Zheng et al. [49]	SJTU (VW)	Conversion into Hsv color space	P → S	Assume existence of specular reflections, maximization of integral projections, integro-differential operator	Iterative shift, shrink and expand circumference process to minimize average intensity
Xu and Shi [46]	CAS-PEAL (VW)	Not described	P → S	Integral projection functions, median filtering, circumference shifting based on average intensity minimization	Sobel filtering, Edges weighting according to position and curvature
Honeywell International [20]	CASIA.1 (NIR)	Not described	P	Search for radial texture discontinuities	-
Dobes et al. [12]	AR, CVL (VW)	Histogram equalization, Gaussian blur	S	-	Canny edges detection, Angular constrained Hough transform
Shuckers et al. [41]	WVU (NIR)	Remove specular reflections (threshold), impainting	P → S	Elliptical integro-differential operator	Elliptical integro-differential operator
Tan et al. [43]	UBIRIS.v1, UBIRIS.v2	Image clustering to perform rough eye localization	P, S	Integro-differential constellation	Integro-differential constellation

studied the image acquisition wavelength of revealed components of the iris, and identified the important role of iris pigmentation.

2.2 Iris Segmentation Methods

Table 1 gives an overview of the main techniques behind several recently published iris segmentation methods. We compare the methods according to the data sets used in the experiments, categorized by the order in which they segment iris borders. The "Experiments" column contains the iris image databases used in the experiments. "Preprocessing" lists the image preprocessing techniques used before segmentation. "Ord. Borders" lists the order in

which the iris borders are segmented, where P denotes pupillary borders and S denotes scleric iris borders ("$x \to y$" denotes the segmentation of y after x and "x, y" denotes independent segmentation). "Pupillary Border" and "Scleric Border" refer to the main methods used to segment any given iris border.

We note that a significant majority of the listed methods operate on NIR images that typically offer high contrast between the pupil and the iris regions, which justifies the order in which the borders are segmented. Also, various innovations have recently been proposed, such as the use of active contour models, either geodesic [40], based on Fourier series [10], or based on the snakes model [2]. These
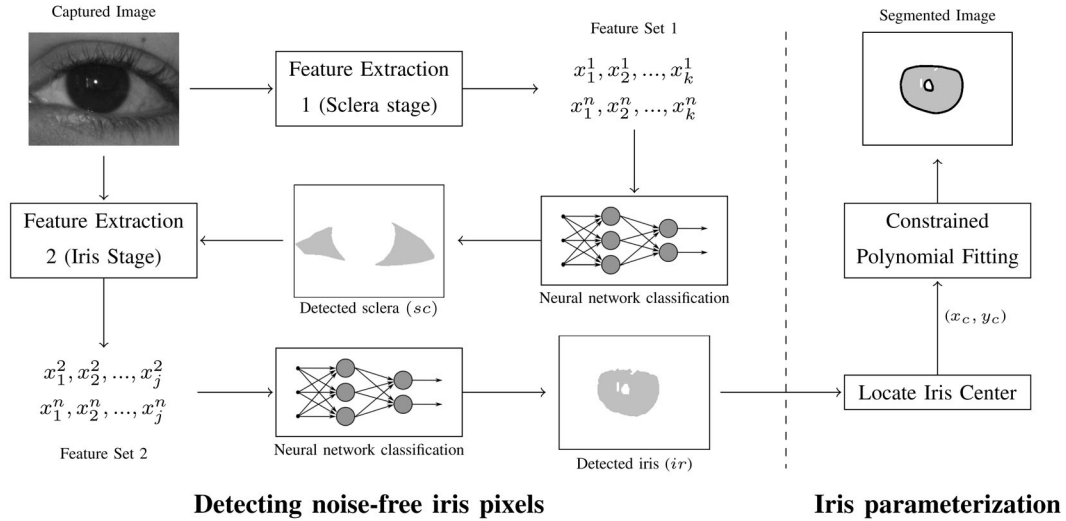
Fig. 3. Block diagram of our iris segmentation method.

techniques require previous detection of the iris to properly initialize contours, and are associated with heavy computational requirements. Modifications to known form fitting methods have also been proposed, essentially to handle off-angle images (e.g., [50] and [44]) and to improve performance (e.g., [23] and [12]). Finally, the detection of noniris data that occludes portions of the iris ring has motivated the use of parabolic, elliptical, and circular models (e.g., [3], and [12]) and the modal analysis of histograms [10]. Even so, in noisy conditions, several authors have suggested that the success of their methods is limited to cases of image orthogonality, to the nonexistence of significant iris occlusions, or to the appearance of corneal reflections in specific image regions.

3 OUR METHOD

Fig. 3 shows a block diagram of our segmentation method, which can be divided into two parts: detecting noise-free iris regions and parameterizing the iris shape.

The initial phase is further subdivided into two processes: detecting the sclera and detecting the iris. The key insight is that the sclera is the most easily distinguishable region in nonideal images. Next, we exploit the mandatory adjacency of the sclera and the iris to detect noise-free iris regions. We stress that the whole process comprises three tasks that are typically separated in the literature: iris detection, segmentation, and detection of noisy (occluded) regions. The final part of the method is to parameterize the detected iris region. In our tests, we often observed small classification inaccuracies near iris borders. We found it convenient to use a constrained polynomial fitting method that is both fast and able to adjust shapes with an arbitrary degree of freedom, which naturally compensates for these inaccuracies.

3.1 Feature Extraction Stages

We used local features to detect the sclera and noise-free iris pixels. Due to performance concerns, we decided to evaluate only those features that a single image scan can capture. Viola and Jones [45] proposed a set of simple

features (reminiscent of Haar basis functions) and computed them over a single image scan with an intermediate image representation. For a given image I, they defined an *integral image*:

$$II(x,y) = \sum_{x'=1}^{x} \sum_{y'=1}^{y} I(x',y'), \qquad (1)$$

where x denotes the image column and y denotes the row. They also proposed a pair of recurrences to compute the integral image in a single image scan:

$$s(x,y) = s(x,y-1) + I(x,y), \qquad (2)$$

$$II(x,y) = II(x-1,y) + s(x,y), \qquad (3)$$

with $s(x,0) = II(0,y) = 0$.

According to this concept, the average intensity (μ) within any rectangular region R_i, delimited by its upper left (x_1, y_1) and bottom-right (x_2, y_2) corner coordinates, is determined by accessing just four array references. Let $T_i = (x_2 - x_1 + 1) \times (y_2 - y_1 + 1)$ be the number of pixels within R_i. Then,

$$\mu(R_i) = \frac{1}{T_i} \left(II(x_2,y_2) + II(x_1,y_1) - II(x_2,y_1) - II(x_1,y_2) \right). \qquad (4)$$

Similarly, the standard deviation (σ) of the intensities within R_i is given by

$$\sigma(R_i) = \sqrt{\mu(R_i^2) - \mu(R_i)^2}, \qquad (5)$$

where $\mu(R_i)$ is given by (4) and $\mu(R_i^2)$ is obtained similarly, starting from an image with squared intensity values. According to (4) and (5), the feature sets used in the detection of the sclera and the noise-free iris regions are central moments computed locally within regions of varying dimensions of different color spaces.

3.2 Sclera Stage

When examining degraded eye images, the iris region can be hard to discriminate, even for humans. Also, the sclera is
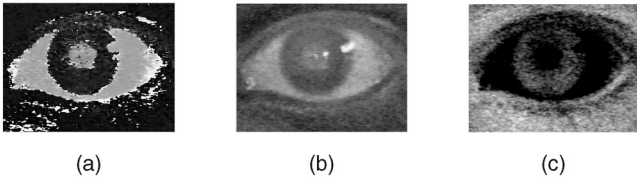
Fig. 4. Discriminating between the regions that belong to the sclera and all the remaining types of information given by the (a) hue, (b) blue chroma (blue—luminance), and (c) red chroma (red—luminance) color components.

much more naturally distinguishable than any other part of the eye, which is a key insight: Our process detects pixels that belong to the sclera and, later, we exploit their mandatory adjacency with the iris in order to find the iris.

Our empirical analysis of different color spaces led to the selection of the hue (h), blue (cb), and red chroma (cr) color components. These serve to maximize the contrast between the sclera and the remaining parts of the eye, as illustrated in Fig. 4. Using the previously described average (4) and standard deviation (5) values, we extracted a 20-dimensional feature set for each image pixel:

$$\{x, y, h_{0,3,7}^{\mu,\sigma}(x,y), cb_{0,3,7}^{\mu,\sigma}(x,y), cr_{0,3,7}^{\mu,\sigma}(x,y)\},$$

where x and y denote the position of the pixel and $h()$, $cb()$, and $cr()$ denote regions (centered at the given pixel) of the hue, blue, and red chroma color components. The subscripts denote the radii used (e.g., $h_{0,3,7}^{\mu,\sigma}(x,y)$ means that six features were extracted from regions of the hue color component: three averages and three standard deviations computed locally within regions of radii 0, 3, and 7).

3.3 Iris Stage

The human eye's morphology dictates that any pixel inside the iris should either have an approximately equal amount of sclera to its left and right if the iris is frontally imaged, or have a much higher value at one of its sides if the iris was imaged off-axis. In any case, the number of sclera pixels in the upper and lower directions should be minimal if the image was acquired from standing subjects without major head rotations.

We used data obtained in the sclera detection stage ("Detected sclera" of Fig. 3) to extract a new type of feature, called "proportion of sclera" $p(x,y)$, for each image pixel. This feature measures the proportion of pixels that belong to the sclera in direction d with respect to the reference pixel (x,y) (in the experiments, the four main directions north $\uparrow$, south $\downarrow$, east $\rightarrow$, and west $\leftarrow$ were used). From (4), the result is given by:

$$p_{\leftarrow}(x,y) = \mu(sc((1,y-1),(x,y))), \quad (6)$$

$$p_{\rightarrow}(x,y) = \mu(sc((x,y-1),(w,y))), \quad (7)$$

$$p_{\uparrow}(x,y) = \mu(sc((x-1,1),(x,y))), \quad (8)$$

$$p_{\downarrow}(x,y) = \mu(sc((x-1,y),(x,h))), \quad (9)$$
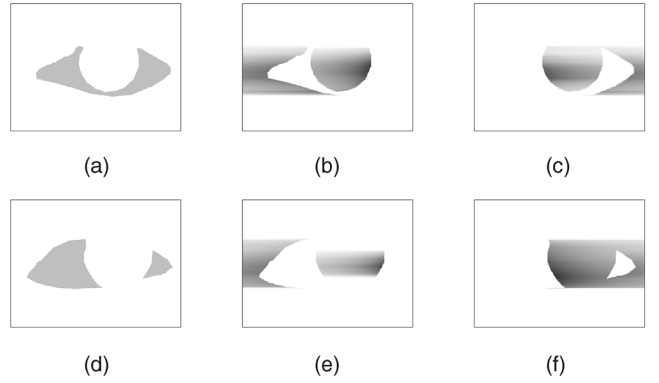
Fig. 5. "Proportion of sclera" values toward the west ($p_{\leftarrow}(x,y)$) and east ($p_{\rightarrow}(x,y)$), obtained from the detected sclera of a frontal (upper row) and an off-angle (lower row) image. For visualization purposes, darker pixels represent higher values. (a) Detected sclera (sc) of a frontal image. (b) Proportion of sclera in the east direction ($p_{\rightarrow}(x,y)$). (c) Proportion of sclera in the west direction ($p_{\leftarrow}(x,y)$). (d) Detected sclera (sc) of an off-angle image. (e) Proportion of sclera in the east direction ($p_{\rightarrow}(x,y)$). (f) Proportion of sclera in the west direction ($p_{\leftarrow}(x,y)$).

where $sc((.,.),(.,.))$ denotes regions of the image that feature the detected sclera (Figs. 5a and 5d), delimited by their top-left and bottom-right corner coordinates. w and h are the image width and height. By definition, the value of $p()$ was set to 0 for all the sclera pixels. Fig. 5 illustrates the $p_{\leftarrow}(x,y)$ and $p_{\rightarrow}(x,y)$ feature values for a frontal image in the upper row and an off-angle image in the lower row. You can see that in both cases, the simple overlap of the feature values almost optimally delimits the iris region.

These "proportion of sclera" values, the pixel position, the local image saturation, and blue chrominance (obtained similarly to the previous feature extraction stage) are computed to yield a 18-dimension feature set:

$$\{x, y, s_{0,3,7}^{\mu,\sigma}(x,y), cb_{0,3,7}^{\mu,\sigma}(x,y), p_{\leftarrow,\rightarrow,\uparrow,\downarrow}(x,y)\}.$$

Again, we selected the color spaces empirically, according to the contrast between the sclera and the iris, as illustrated in Fig. 6. $s()$ and $cb()$ denote regions of the saturation and blue chrominance color components. As in the previously described feature extraction stage (sclera detection), the subscripts give the radii we used, centered at the given pixel.

3.3.1 Adaptability to Near-Infrared Images

Both of the feature extraction stages we described use information about pixel color (hue, red, and blue chroma). As this information is not available in single channel NIR images, we thought it would be useful to adapt both feature extraction stages to this type of data. In this situation, all of the features were extracted from the intensity image and
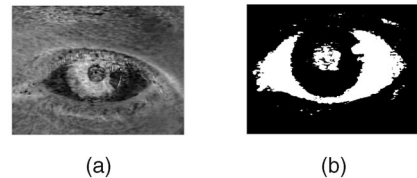
Fig. 6. Color components used in iris detection. (a) Saturation color component. (b) Blue chroma color component.
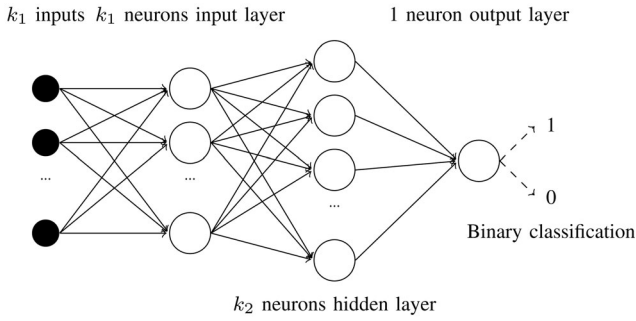
Fig. 7. Schema for the multilayered feed-forward neural networks used in both classification stages of our segmentation method.

computed locally at five different radii values, yielding 12 feature values per image pixel in the sclera detection stage and 16 in the iris detection stage. The feature set used in sclera detection consists of: $\{x, y, i_{0,3,5,7,9}^{\mu,\sigma}(x,y)\}$, where x and y denote the position of the pixel and $i()$ denotes regions (centered at the given pixel) of the intensity image. Again, the subscripts denote the radii of such regions. Iris detection is based on the following set of features: $\{x, y, i_{0,3,5,7,9}^{\mu,\sigma}(x,y), \ p_{\leftarrow,\rightarrow,\uparrow,\downarrow}(x,y)\}$, where $p()$ denotes the above-defined proportion of sclera features.

3.4 Supervised Machine Learning and Classification

Both classifiers in our method operate at the pixel level and perform binary classification. For these, we evaluated several alternatives according to three fundamental learning theory issues: model capacity, computational complexity, and sample complexity. We were mindful of heterogeneity and the amount of data available for learning purposes, which justified the use of neural networks. We know that these types of classifiers can form arbitrarily complex decision boundaries. Thus, the model capacity is good. Also, the back-propagation learning algorithm propitiates good generalization capabilities using a relatively small amount of learning data.

As shown in Fig. 7, we used multilayered perceptron feed-forward neural networks with one hidden layer for both classification stages, not considering the input nodes as a layer. All of the networks feature as many neurons in the input layer (k_1) as the feature space dimension (k_2) neurons in the hidden layer and a single neuron in the output layer.

As transfer functions, we used the sigmoid hyperbolic tangent on the first two layers and pure linear on the output. Several parameters affect the networks' results, such as the number of neurons used in the hidden layer, the amount of data used for learning, and the learning algorithm. During the experimental period, we varied most of these parameters, to arrive at the optimal values as reported in Section 4.

3.5 Shape Parameterization

Efficient shape parameterization is a key issue for post-segmentation recognition stages. With a set of image pixels that are classified as *noise-free iris*, the goal is to parametrically approximate the contour of the pupillary and scleric iris borders. Recently, researchers have proposed using active contour and spline techniques for this type of task, although they were not considered the most convenient for the purposes of our work, essentially due to performance concerns. Instead, we performed a polynomial regression on a polar coordinate system, which runs naturally fast and compensates for inaccuracies from the previous classification stage, as illustrated in Fig. 8. The process starts by roughly localizing the iris center. The center serves as a reference point in the translation into a polar coordinate system, where we perform the polynomial regression. Remapping the obtained polynomials into the original Cartesian space gives the parameterization of the pupillary and scleric iris borders.

The iris and pupil are not concentric, although their centers are not distant from one another. We identify a pixel (x_c, y_c) that roughly approximates these centers and use it as a reference point. Let B be a binary image that distinguishes between the noise-free iris regions and the remaining types of data (Fig. 5d). Let $C = \{c_1, \ldots, c_w\}$ be the cumulative vertical projection of B, and $R = \{r_1, \ldots, r_h\}$ be the horizontal projection, that is, $c_i = \sum_{j=1}^{h} B(i,j)$ and $r_i = \sum_{j=1}^{w} B(j,i)$. Since the iris regions are darker, the values of c_i and r_i decrease in the rows and columns that contain the iris, as illustrated in Fig. 9.

Let $C^* = \{c_{1^*}, \ldots, c_{m^*}\}$ be a subset containing the first-quartile elements of C_i and $R^* = \{r_{1^*}, \ldots, r_{n^*}\}$ be a subset containing the first-quartile elements of R_i which correspond to the darkest columns and lines of the binary image. An approximation to the iris center (x_c, y_c) is given by the median values of C^* and R^*: that is, $x_c = c_{\frac{m^*}{2}}$ and $y_c = c_{\frac{n^*}{2}}$. We measure the distance between (x_c, y_c) and the pixels
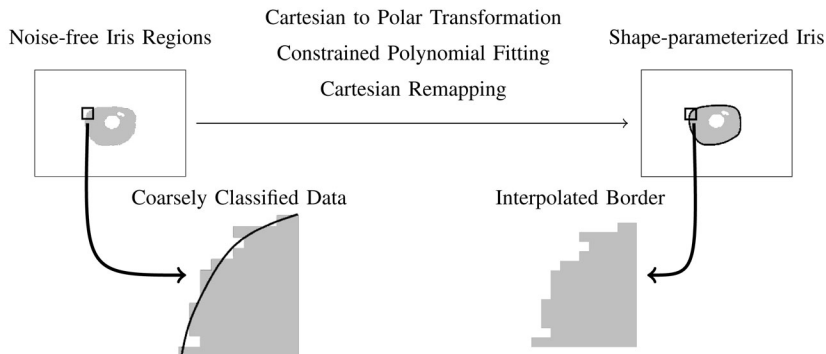
Fig. 8. Parameterizing segmented noise-free iris regions through constrained polynomial fitting techniques.
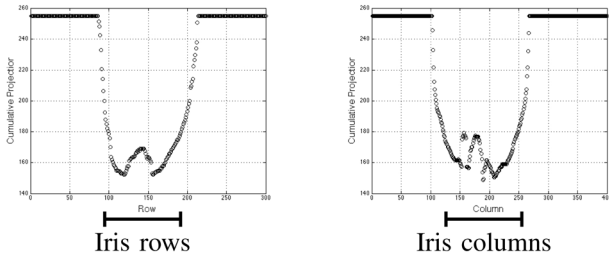
Fig. 9. Horizontal and vertical cumulative projections of the iris image (ir) illustrated in Fig. 8.

classified as *iris* along θ_i directions, such that $\theta_i = \frac{i2\pi}{t}$, $i = 1, \ldots, t-1$. The highest value in each direction approximates the distance between the contour of the iris and the reference pixel (x_c, y_c), as illustrated in Figs. 10a and 10b (Cartesian and polar coordinate systems). A set of simple semantic rules keeps incompletely closed pupil or iris shapes from degrading the process. The simplest rule is that contour points should be within the interval $[l_1, l_2]$. The regression procedure discards values outside this interval.

Hereafter, we regard the problem as a polynomial regression. We could use other shape-fitting techniques at this stage with similar results, but we chose this approach for its lower computational requirements. Given a set of t data points (x_i, y_i), the goal is to optimize the parameters of a kth degree polynomial $p(x) = a_0 + a_1 x + \cdots + a_k x^k$ so as to minimize the sum of the squares of the deviations S^2:

$$S^2 = \sum_{i=1}^{t} (y_i - p(x_i))^2, \tag{10}$$

where y_i is the desired value at x_i and $p(x_i)$ is the response value at x_i. To guarantee a closed contour of the iris border in the Cartesian coordinate system, we must ensure that $p(x_1) = p(x_t)$, which gives rise to an equality constrained least squares problem [15]. The goal is to find a vector $x \in R^k$ that minimizes $\|Ax - b\|_2$, subject to the constraint $Bx = d$, assuming that $A \in R^{m \times k}$, $B \in R^{p \times k}$, $b \in R^m$, $d \in R^p$, and $rank(B) = p$. Here, A refers to the iris boundary points that are to be fitted and B is the constraint that guarantees a closed contour. Considering that the null spaces of A and B intersect only trivially, this problem has a unique solution, x^*. As Loan describes [24], a possible solution is obtained through the elimination method, which uses the constraint equation to solve for m elements of b in terms of the

remaining ones. The first step to the solution is to find an orthogonal matrix Q such that $Q^T B^T$ is upper triangular:

$$Q^T B^T = \begin{bmatrix} R_B \\ 0 \end{bmatrix}. \tag{11}$$

Next, we solve the system $R_B^T y_1 = d$ and set x_1 to $Q_1 y_1$, where $Q = [Q_1 Q_2]$, $Q_1 \in R^p$, and $Q_2 \in R^{k-p}$. Again, we find an orthogonal matrix U such that $U^T(AQ_2)$ is upper triangular:

$$U^T(AQ_2) = \begin{bmatrix} R_A \\ 0 \end{bmatrix}. \tag{12}$$

We set $R_A y_2 = U_1^T(b - Ax_1)$ and $x_2 = Q_2 y_2$, where $U = [U_1 U_2]$, $U_1 \in R^{k-p}$, and $U_2 \in R^{m-k+p}$. Finally, the solution is given by

$$x^* = x_1 + x_2. \tag{13}$$

3.6 Computational Complexity

As noted previously, the computational complexity of the given segmentation method is a major concern for real-time data handling. The first part of the method operates at the pixel level, and all the corresponding operations receive as input all the image pixels: either their RGB, intensity, or feature vectors. Let I be a RGB image with $n = c \times r$ pixels (typically $120,000 = 400 \times 300$ in the experiments). Given this relatively large value, we must maintain an asymptotic upper bound on execution time that is linear in the size of the input, ensuring that the first stage of the method (and the most time consuming) runs quickly. Thereafter, the parameterization of the iris borders depends on the number of directions from which reference points are picked and on the polynomial degree. As these values are relatively low (in our experiments, the number of directions is 64 and the degree is 10), increased computational complexity is not a concern since it will not significantly lower the method's performance. Also, as we discuss in Section 4.5, we emphasize that our method offers roughly deterministic performance, that its performance is linear in image size, and that it is significantly faster than other segmentation methods for similar scenarios.

4 EXPERIMENTS

We describe two types of experiments. We performed the first type while developing our method. This type is related to the main configuration parameters (network topology, learning algorithm, and polynomial degree), and we tuned
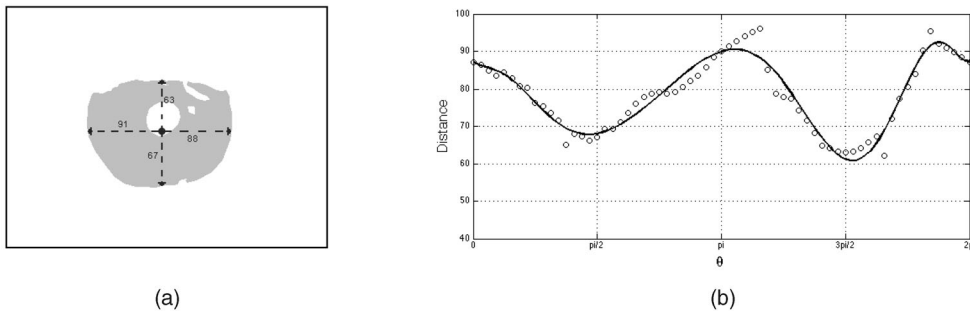
Fig. 10. Greatest distances between the iris center and the pixels classified as *iris* along θ directions (a) in the Cartesian coordinate system, 4 directions, and (b) in the polar coordinate system, 64 directions. The continuous line gives the 10th degree constrained polynomial for the purposes of data regression.

(a)

(b)
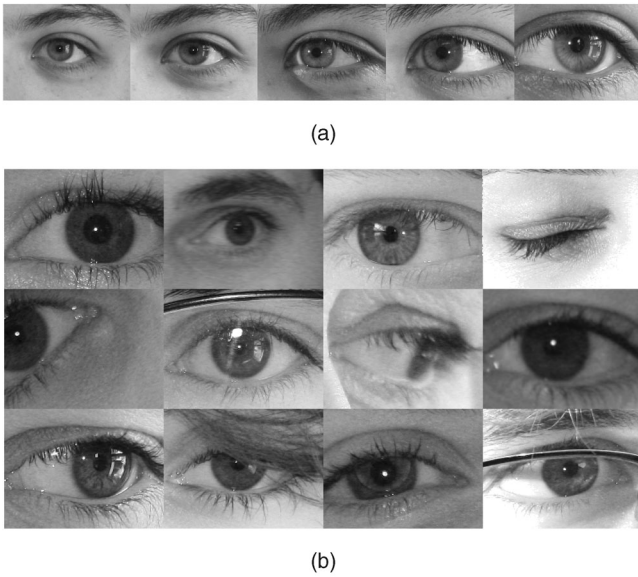
Fig. 11. Examples of images acquired at large varying distances (between 4 and 8 meters) from moving subjects and under dynamic lighting conditions (UBIRIS.v2 database). (a) Sequence of images taken on the move and at a distance. (b) Degraded images from the UBIRIS.v2 database.

it exclusively to the UBIRIS.v2 data set. Later, to contextualize our results, we compared our method's performance with that of three state-of-the-art segmentation strategies across three well-known data sets (Face Recognition Technology (FERET) [33], Face Recognition Grand Challenge (FRGC) [34], and ICE [30]).

4.1 Development Data Set

As illustrated in Fig. 11a, the significantly higher range of distances between the subjects and the imaging framework (between 4 and 8 meters, Fig. 11a) is a major distinguishing point between the UBIRIS.v2 data set and others with similar purposes. Through visual inspection, 14 ways to degrade images were detected and classified into one of the two classes: *local* or *global*, according to whether they affect image regions alone or the entire image. The first class comprises iris occlusions (eyelids, eyelashes, hair, glasses, specular, and lighting (ghost) reflections), nonlinear deformations due to contact lenses, and partial images, while the latter comprises poorly focused, motion-blurred, rotated, off-angle, improper lighting, and out-of-iris images (that is, images without any portion of the iris texture visible). Fig. 11b compares a high-quality close-up iris image (the upper left image) with degraded iris images.

The known good control data comprises 1,000 manually made binary maps that distinguish between noise-free iris regions and all of the remaining types of data in the UBIRIS.v2 images. We also created 1,000 binary images that segment the sclera manually, in order to better understand which classifiers should be used in the sclera detection stage. Images measure 400×300 pixels, yielding a total of 120,000,000 pixels for the whole data set.

4.2 Learning Algorithms

The learning stages of the sclera and iris classifiers use a back-propagation strategy. Initially, this learning strategy updates the network weights and biases it in the direction of the negative of the gradient, that is, the direction in which the performance function E decreases most rapidly. E is a squared error cost function given by $\frac{1}{2}\sum_{i=1}^{p} \|y_i - d_i\|^2$, p is the number of learning patterns, y_i is the network's output, and d_i is the desired output. There are many variations of the back-propagation algorithm, which essentially improve learning performance by a factor of between 10 and 100. Typical variants fall into two classes: The first uses heuristic techniques, such as the momentum or variable learning rates. The second category uses standard numerical optimization methods, for example, search across the conjugate directions (with Fletcher-Reeves [14] or Powell-Beale [36] updates) or quasi-Newton algorithms (Broyden, Fletcher, Goldfarb, and Shanno [11] and one-secant [4] update rules) that, although based on the Hessian matrix to adjust values, do not require the calculation of second derivatives.

The neural network we use has three parameters that determine its final accuracy: the learning algorithm, the amount of learning data, and the network topology. To avoid an exhaustive search for the optimal configuration, we first chose the back-propagation learning algorithm. We built a set of neural networks with an a priori reasonable topology (three layers with the number of neurons in the input and hidden layers equal to the dimension of the feature space), and we used 30 images in the learning set, from which we selected 50,000 instances (pixels) randomly, equally divided between positive (iris) and negative (noniris) samples. Table 2 lists our results. "Learning Error" columns list the average errors recorded in the learning stages, "Time" the average computational time for the learning processes (in seconds), "Classification Error" the average error obtained across the test set images. "Sc" denotes the sclera classification stage, and "Ir" denotes the iris classification stage. All of the values are expressed in confidence intervals of 95 percent. These experiments led to the selection of the Fletcher-Reeves [14] learning method for the back-propagation algorithm and to its use in all subsequent experiments.

TABLE 2
Comparison between the Average Error Rates (from the Learning and Classification Stages)
of the Variants of the Back-Propagation Algorithm Used in Our Experiments

Learning Algorithm	Time (Sc)	Learning Error (Sc)	Classification Error (Sc)	Time (Ir)	Learning Error (Ir)	Classification Error (Ir)
Fletcher-Reeves [14]	2808 ± 7.35	$0.027 \pm 2.1E^{-4}$	$0.029 \pm 2.7E^{-4}$	3320 ± 8.98	$0.020 \pm 1.8E^{-4}$	$0.021 \pm 1.8E^{-4}$
Powell-Beale [36]	2751 ± 8.20	$0.026 \pm 2.3E^{-4}$	$0.029 \pm 2.7E^{-4}$	3187 ± 9.30	$0.020 \pm 2.0E^{-4}$	$0.022 \pm 2.1E^{-4}$
Broyden *et al.* [11]	4807 ± 9.14	$0.026 \pm 3.2E^{-4}$	$0.031 \pm 3.5E^{-4}$	5801 ± 10.52	$0.019 \pm 2.7E^{-4}$	$0.023 \pm 2.9E^{-4}$
One-secant [4]	2993 ± 7.13	$0.030 \pm 2.2E^{-4}$	$0.034 \pm 2.4E^{-4}$	3491 ± 8.61	$0.024 \pm 2.0E^{-4}$	$0.031 \pm 2.1E^{-4}$

(a)

(b)
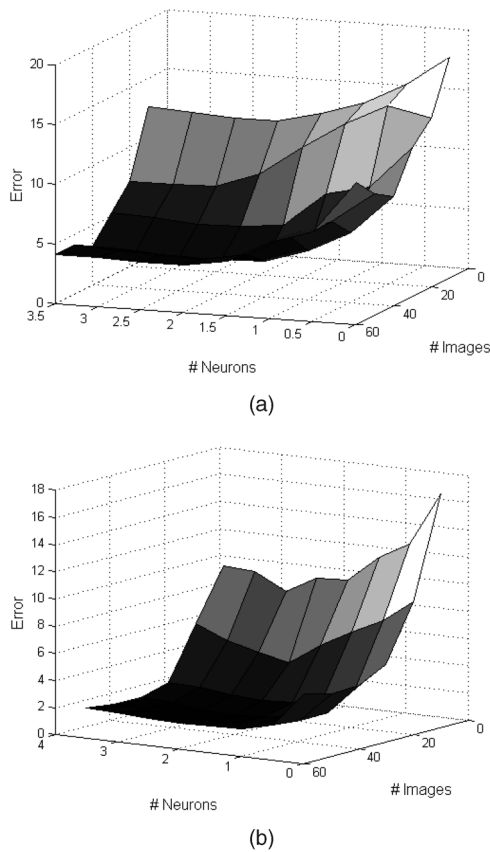
Fig. 12. Error rates obtained with the UBIRIS.v2 data set, for the number of images used in the learning stage ("#Images") and the number of neurons in the network hidden layer ("#Neurons," expressed in the feature space dimension). The error values are percentiles and averaged over 20 neural networks with the given configuration. (a) Error rates in the sclera classification stage. (b) Error rates in the iris classification stage.

4.3 Learning Sets and Network Topology

Fig. 12 shows two 3D graphs that give the error rates obtained on the test data set, according to the number of images used in the training set ("#Images") and the proportion between the feature space dimension and the number of neurons used in the networks' hidden layers ("#Neurons"). The error values are averages from 20 neural networks and are expressed as percentages. We note that error values correspond directly to the number of neurons and to the number of images used to learn. Also, we observed that error values stabilize when more than 40 images are used in the learning set and when the number of neurons in the hidden layer is 1.5 times higher than the feature space dimension. We confirmed this conclusion with both the sclera and the iris classification models.

Interestingly, we recorded the lowest error rates in the iris classification stage, which can be explained by the useful information provided by the previous classification stage, which lessens the difficulty of this task. The lowest iris classification error was about 1.87 percent, which—based on visual inspection of the results—was considered very acceptable. This gives about 2,244 misclassified pixels per image, a number that can be reduced by basic image processing methods. For instance, morphologic operators should eliminate small regions of *iris* that are not contiguous with the largest iris region and would otherwise cause errors.
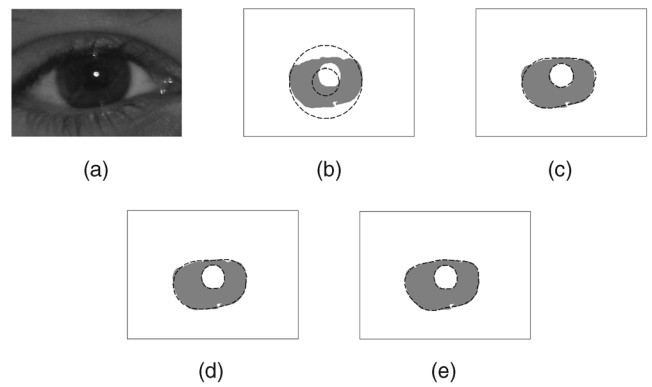
Fig. 13. Variability of the shapes that parameterize the iris borders consistent with the degree of the interpolating polynomial. (a) Close-up iris image. (b) Fitted polynomial (1 degree). (c) Fitted polynomial (5 degrees). (d) Fitted polynomial (10 degrees). (e) Fitted polynomial (15 degrees).

4.4 Iris Border Parameterization

Evaluating the goodness-of-fit of any parametric model is a major issue in fitting functions. Here, we assume there should exist a polynomial relationship between the independent and dependent variables. As illustrated in Fig. 13, the degree of the interpolating polynomials dictates the shape of the segmented iris border. Here, an iris image with upper and lower extremes occluded by eyelashes and eyelids exhibits a far-from-circular noise-free iris shape. The subsequent figures give the shapes of the segmented iris borders, according to the degree of the fitted polynomials.

An objective measure for the goodness-of-fit is the R^2 value, equal to

$$R^2 = 1 - \frac{\sum (y_i - \hat{y}_i)^2}{\sum (y_i - \bar{y})^2}, \qquad (14)$$

where y_i are the desired response values, $\hat{y}_i$ the polynomial response values, and $\bar{y}$ the average of y_i. Fig. 14 gives the average R^2 values for the scleric (continuous line with circular data points) and pupillary (dashed line with cross data points) iris borders. We note that the values tend to stabilize when the degree of the polynomial is higher than 6 and remain practically constant for degrees higher than 10. Also, keep in mind that higher R^2 values do not always
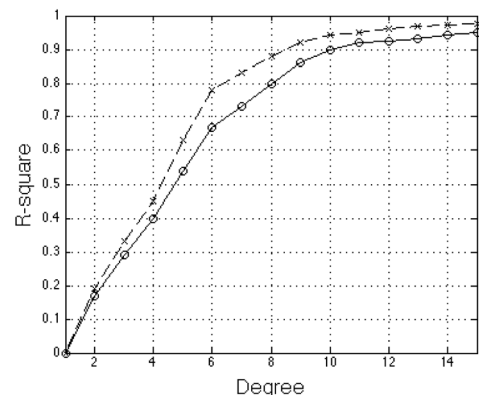
Fig. 14. Obtained R^2 values for the degree of the fitted polynomials in the scleric (continuous line with circular data points) and pupillary (dashed line with cross data points) iris borders.
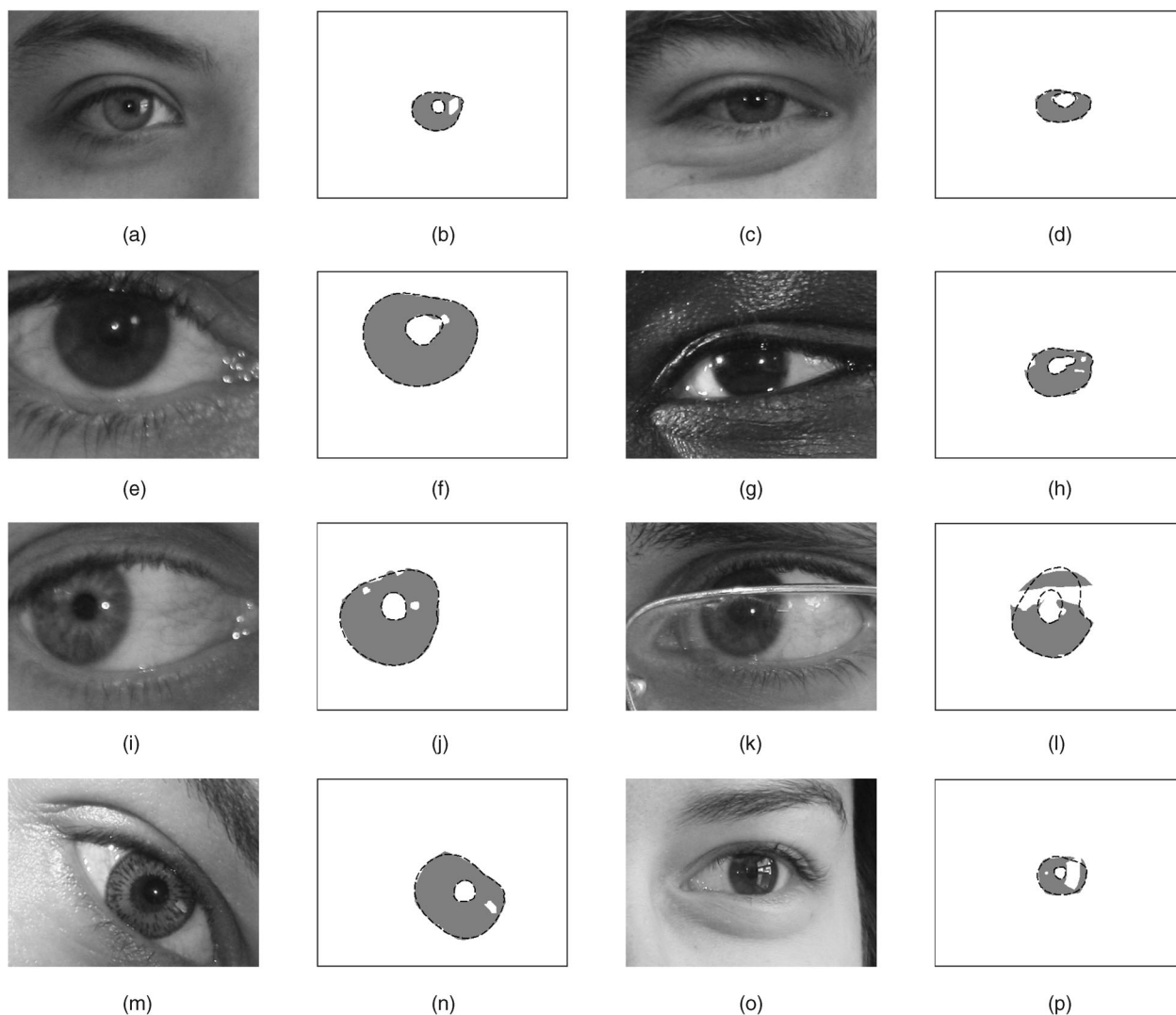
Fig. 15. Examples of the results achieved by our segmentation method on visible wavelength images from the UBIRIS.v2 database. Noise-free iris pixels appear in gray and the iris borders are black dashed lines. (a) Example of a close-up iris image. (b), (d), (f), (h), (j), (l), (n), and (p) Segmentation results. (c) Heavily occluded iris image. (e) Heavily pigmented iris. (g) Black subject. (i) Off-angle iris image. (k) Iris occluded by glasses. (m) Rotated eye. (o) Iris occluded by reflections.

indicate better iris borders, as the polynomial fitting procedure was chosen to smooth the data and compensate for classification inaccuracies near the iris borders.

Fig. 15 illustrates the results obtained for the UBIRIS.v2 images, where the noise-free iris data appear in gray and the iris borders are represented with dashed black lines. The visual plausibility of the results is evident, either for images within a large range of acquisition distances (8 meters, Figs. 15b and 15d, and 4 meters, Figs. 15f and 15j), different levels of iris pigmentation (light, Figs. 15j and 15n, and heavy, Figs. 15h and 15p), with large iris occlusions (Figs. 15l and 15p), and on off-angle (Fig. 15j), poor focused (Fig. 15f), and rotated (Fig. 15n) eyes. The method was suitable to segment noncontiguous iris data in the context of severe iris occlusions, as exemplified in Figs. 15k and 15l.

4.5 Contextualizing Results and Data Dependencies

We elected to compare our results with three state-of-the-art iris segmentation strategies on four well-known data sets: the VW color UBIRIS.v2, FERET [33] and FRGC [34], and the NIR ICE [30]. The first method we chose for comparison was the integrodifferential operator [9], due to its prominence in the iris recognition literature. We used elliptical shapes to detect the iris, and parabolic shapes to detect eyelid borders. The second method was the active contour approach based on discrete Fourier series expansions [10] (with 17 activated Fourier components to model the inner iris boundaries and 5 to model the outer boundaries), and the detection of eyelashes through a modal analysis of the intensity histogram. Finally, we used the proposal of Tan et al. [43] (detailed in Table 1), which achieved the best results in a recent international iris segmentation contest.[1] We note that this is not a completely fair comparison for the integrodifferential and active contour-based strategies, as they are only designed to handle NIR images. The results from the color data sets are solely for comparison and to confirm that, although highly efficient for NIR images, these algorithms cannot handle VW degraded data. Also, we

1. NICE.I: http://nice1.di.ubi.pt.
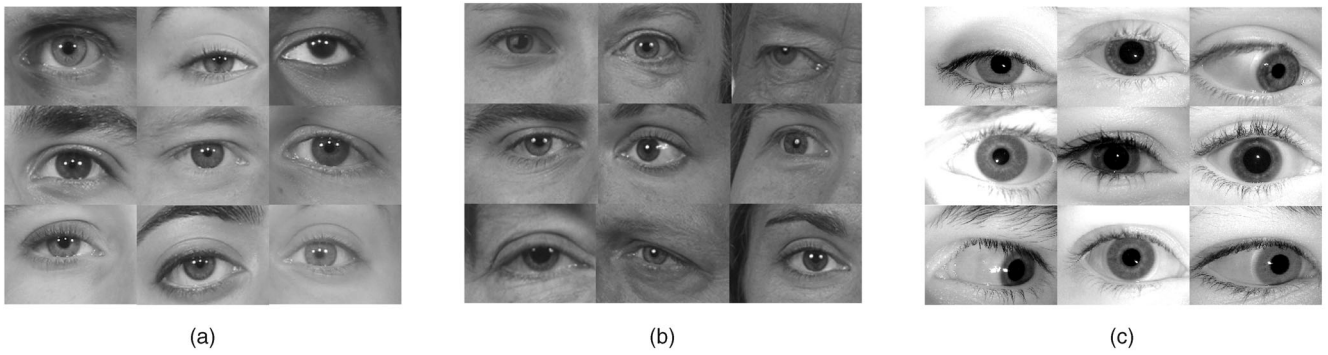
Fig. 16. Other databases used in the experiments. (a) Images from the FRGC database. (b) Images from the FERET database. (c) NIR images from the ICE (2006) database.

stress that all of the parameters previously tuned for the method given in this paper were preserved: Specifically, we consistently used neural networks with topologies $20 : 35 : 1$ and $18 : 27 : 1$ in the sclera and iris classification stages, the Fletcher-Reeves back-propagation learning algorithm, 50,000 pixels randomly selected from the learning data and fitted polynomials with degree 10. Finally, the images used for learning and testing are completely separable, in a twofold cross-validation schema.

The data set used in the FRGC was collected at the University of Notre Dame and contains images with varying definition, taken under both controlled and un-controlled lighting conditions. We selected a subset (500) of the higher definition images and manually cropped and resized the eye regions, obtaining a set of images illustrated

in Fig. 16a. These are degraded for several reasons (poorly focused, occluded irises, and large reflection areas). The FERET database is managed by the US Defense Advanced Research Projects Agency and the US National Institute of Standards and Technology. It contains 11,338 facial images from 994 subjects over multiple imaging sessions. Again, we selected a subset of images (500) and cropped and resized the eye regions manually, obtaining images similar to those in Fig. 16b. Finally, we selected 500 images from the ICE (2006) data set, as illustrated in Fig. 16c. For all of the data sets, we manually created the corresponding binary maps that localize the iris and the sclera.

Fig. 17 shows segmentation results output by our method on the FRGC, FERET, and ICE data sets. The procedure adopted for the FERET and FRGC images was
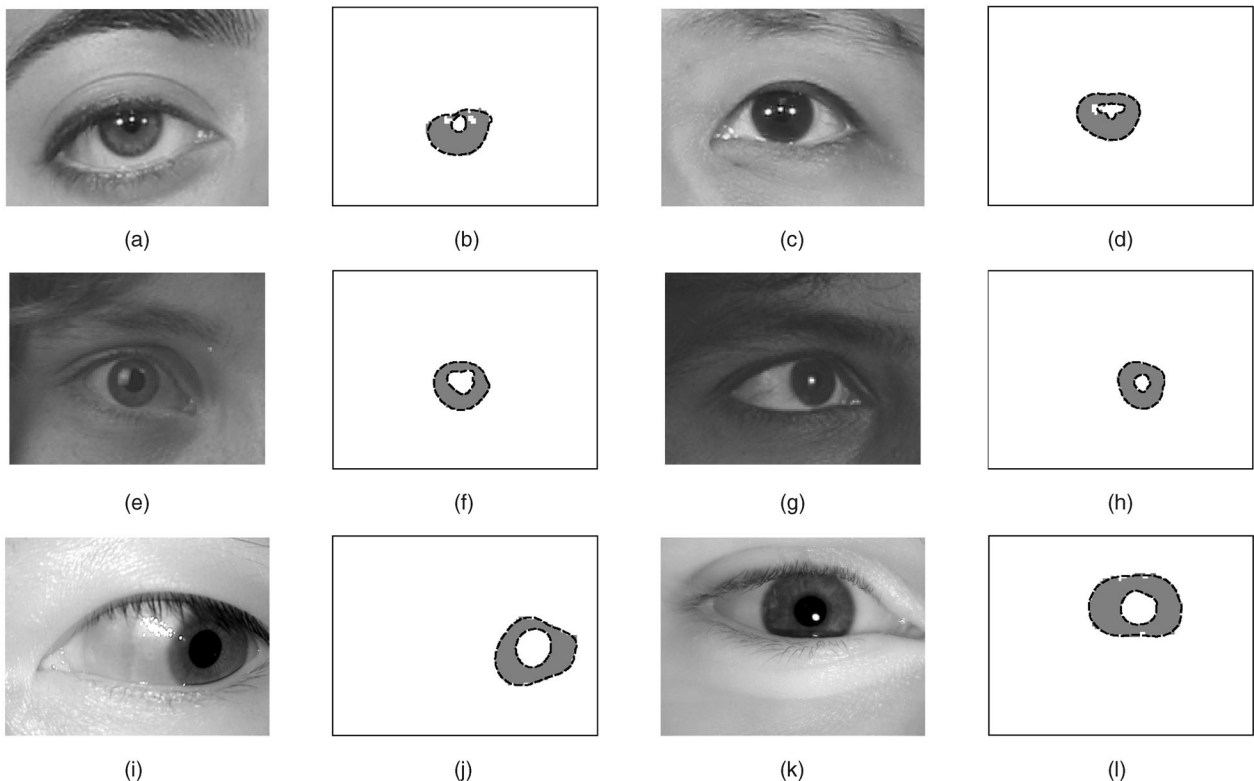
Fig. 17. Examples of the results achieved by our segmentation method on the FRGC (upper row), FERET (middle row), and ICE (lower row) databases. (a) Heavily occluded FRGC image. (b), (d), (f), (h), (j), and (l) Segmentation results. (c) Heavy pigmented FRGC image. (e) Lightly pigmented iris FERET image. (g) Heavily pigmented iris FERET image. (i) Off-angle ICE image. (k) Occluded ICE image.
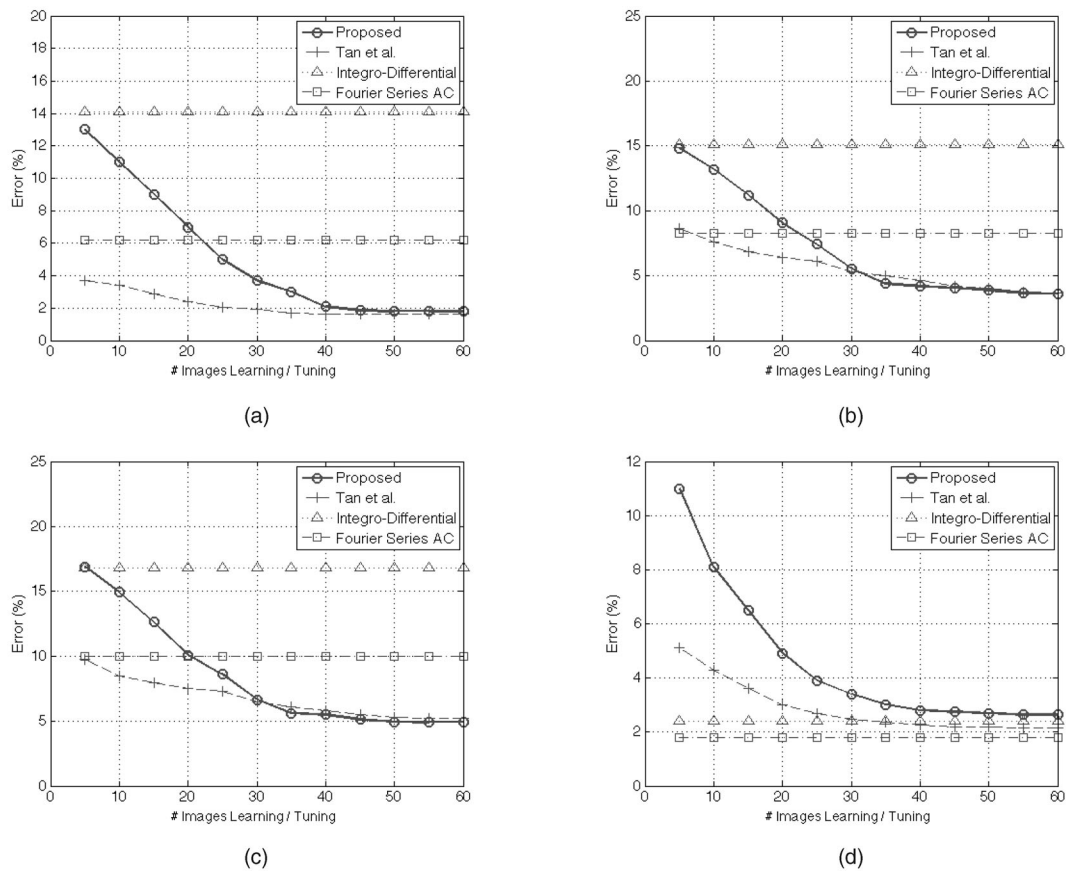
Fig. 18. Results obtained using the four tested segmentation strategies on the UBIRIS.v2, FRGC, FERET, and ICE (2006) data sets. (a) UBIRIS.v2 images, (b) FRGC images, (c) FERET images, and (d) ICE (2006) images.

similar to that used for UBIRIS.v2, while for the ICE data we made changes to the NIR images described in Section 3.3.1. For all of the tested data sets, we observed that—most of the time—our method segmented the noise-free iris data in a visually acceptable way.

Fig. 18 quantitatively compares the error rates obtained by the four segmentation methods we tested on each of the above-mentioned data sets. Our method is denoted by continuous lines with circular data points, the integrodifferential operator by dotted lines with triangular data points, and the active contour approaches by the dash-dotted line with square data points. Finally, the proposal of Tan et al. is denoted by the dashed line series with cross data points. The horizontal axis gives the number of images used in the learning stages of our method and in the tuning of Tan et al.'s parameters. The vertical axis gives the percentage of misclassified pixels (to contextualize these values and relate them with the intuitive acceptability of the

segmentation result, Fig. 19 shows a segmented image that illustrates the percentage of misclassified pixels between 1 and 5 percent). We note the pronounced deterioration of the results obtained by the integrodifferential and active contour methods on the VW degraded data sets. Although their effectiveness on the NIR images is clear, they encountered problems in handling the higher data heterogeneity of these data: specifically, the many types of noise factors that occlude regions inside the iris texture and make it difficult to tune the active contour convergence criterion. This underscores the exclusive suitability of these well-known segmentation strategies to deal with images acquired under constrained acquisition conditions. The results from our method and the method of Tan et al. were usually very similar for the VW color data sets. However, the method of Tan et al. may better handle NIR images and clearly achieved error rates comparable to the active contour approach. This is to be expected because the latter
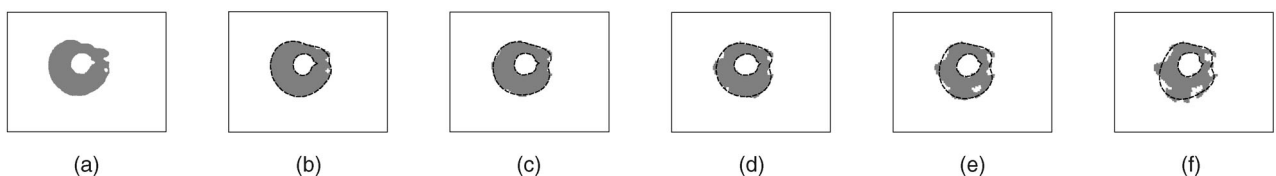
Fig. 19. Illustration of the segmentation results, according to the percentage of misclassified pixels. (a) Ground truth segmentation. (b) Segmentation error 1 percent. (c) Segmentation error 2 percent. (d) Segmentation error 3 percent. (e) Segmentation error 4 percent. (f) Segmentation error 5 percent.

TABLE 3
Comparison of the Best Results Obtained by Our Method, the Elliptical Integrodifferential Operator,
and Two State-of-the-Art Segmentation Techniques

Data Set	UBIRIS.v2	FRGC	FERET	ICE(2006)
Segmentation Method	Error [%] (Time [s])	Error [%] (Time [s])	Error [%] (Time [s])	Error [%] (Time [s])
Our method	$1.87 \pm 2.4E^{-3}$ (0.78 ± 0.01)	$4.33 \pm 3.6E^{-3}$ (0.78 ± 0.01)	$4.61 \pm 3.7E^{-2}$ (0.78 ± 0.01)	$2.66 \pm 2.9E^{-3}$ (0.70 ± 0.01)
Integro-differential [9]	$13.97 \pm 6.2E^{-3}$ (2.73 ± 0.01)	$15.1 \pm 6.4E^{-3}$ (2.73 ± 0.01)	$16.83 \pm 6.7E^{-2}$ (2.73 ± 0.01)	$2.39 \pm 3.4E^{-3}$ (2.73 ± 0.01)
Fourier active contours [10]	$6.20 \pm 4.3E^{-3}$ (3.90 ± 0.18)	$8.10 \pm 4.9E^{-3}$ (4.66 ± 0.18)	$9.96 \pm 5.3E^{-2}$ (4.69 ± 0.11)	$1.79 \pm 2.3E^{-3}$ (4.41 ± 0.13)
Tan *et al.* method [43]	$1.72 \pm 2.3E^{-3}$ (5.08 ± 0.16)	$4.20 \pm 3.6E^{-3}$ (5.03 ± 0.14)	$5.02 \pm 3.9E^{-2}$ (5.01 ± 0.09)	$2.26 \pm 2.6E^{-3}$ (4.80 ± 0.13)

method exclusively analyzes the red component of VW color images and the use of the NIR data does not demand significant changes, as opposed to our method.

Table 3 summarizes the best results obtained by each segmentation strategy and the corresponding average computation time (in seconds). The error rates are percentiles and correspond to 95 percent confidence intervals. From this analysis, the lower computational requirements of the proposed method are clear: Our method runs extremely fast and in practically deterministic time, taking less than a second per image, even using an interpreted programming language and an integrated development environment. This is almost one order of magnitude faster than the method that achieved comparable error rates on the VW data sets. Also, appropriate code optimization and porting to a compiled language should make the method

suitable for real-time data. Note that the above results were obtained when we used the same type of data set (albeit a separable one) for learning and test purposes.

To assess the data dependence of our method, we calculated the following results when we used different types of the VW databases for learning and testing. Fig. 20 shows four plots that quantify the obtained error rates, where $x \rightarrow y$ in the upper right corner of each plot means that the x database was used for learning and y for testing. Fig. 20a illustrates the results obtained when using one of the databases exclusively for learning and a test set that was derived from each of the different databases (denoted *). We note that the error rates tend to stabilize when a larger number of images were used in the training stage (over 60 images) and that the results were better when UBIRIS
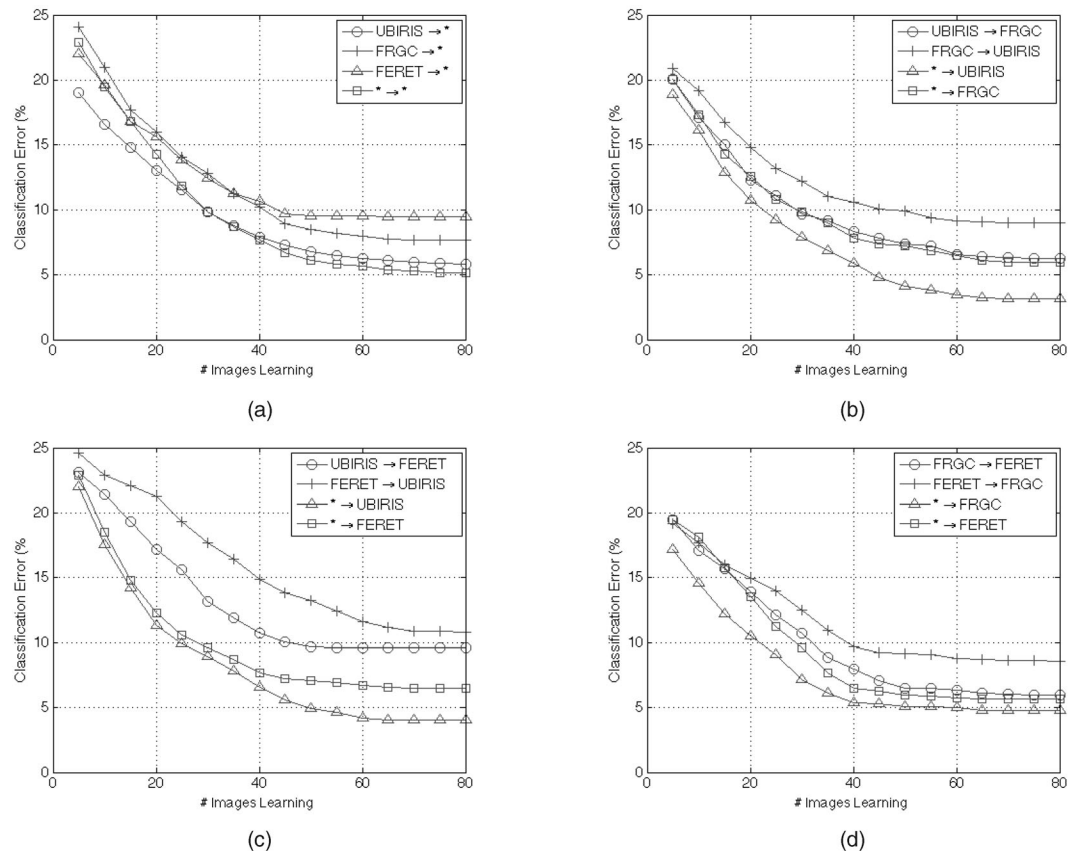
Fig. 20. Data dependence of our segmentation method. (a) Multiple database evaluations. (b) Learning/test in the UBIRIS and FRGC data sets. (c) Learning/test in the UBIRIS and FERET data sets. (d) Learning/test in the FRGC and FERET data sets.

images were used for learning. This is justified by the higher definition of the UBIRIS.v2 data, compared with the other data sets, which yields an excess of information that is useful for learning purposes. The lowest error rates (5.02 percent) were obtained when either the learning data or the test data were derived equally from all of the VW data sets. This yielded a deterioration of about 3.14 percent as compared to the better results. A slightly higher error value (5.85 percent) was obtained when the learning data consisted solely of UBIRIS.v2 images and the test data were derived equally from each of the three data sets.

Figs. 20b, 20c, and 20d illustrate the results obtained when using images of the UBIRIS.v2/FRGC, UBIRIS.v2/FERET, and FRGC/FERET data sets in the learning and test stages. Again, the * symbol denotes a set derived from each of the given data sets. Not surprisingly, better results were generally obtained when the learning data comprised images from all the databases. Also, the error rates were generally lower when the database with higher definition data was included in the learning set, as seen from the plots of $UBIRIS \rightarrow FRGC$ and $FRGC \rightarrow UBIRIS$ (Fig. 20b) and $UBIRIS \rightarrow FERET$ and $FERET \rightarrow UBIRIS$ (Fig. 20c). The greatest difference in resolution is between the UBIRIS.v2 and FERET images, which explain the higher error rates obtained when these data sets were mixed, in comparison with the results obtained for the UBIRIS.v2/FRGC and FRGC/FERET data sets. The average deterioration of the results when the learning and the test data did not contain the same type of data was about 1.83, 0.57, and 1.29 percent, respectively, for the UBIRIS.v2, FRGC, and FERET data sets. However, we note that the characteristics of the data sets are very different and that the adjustment of any parameter in such heterogeneous data is highly challenging in any situation. We concluded that including multiple types of data in the learning set would not be an obvious problem for our method's effectiveness, even though its inclusion would lower the resulting effectiveness. Also, we stress that the major method configuration parameters (network topology, neuronal transfer functions, and number of instances used to learn) were not adjusted during any of the experiments.

5 CONCLUSIONS

Due to favorable comparisons with other biometric traits, the popularity of the iris has grown considerably and efforts are concentrated in the development of systems that are less constrained to subjects, using images captured at-a-distance and on-the-move. These are extremely ambitious conditions that lead to severely degraded image data, which can be especially challenging for image segmentation.

Our method encompasses three tasks that are typically separated in the literature: eye detection, iris segmentation, and discrimination of the noise-free iris texture. Our key insight is 1) to consider the sclera as the most easily distinguishable part of the eye in the case of degraded images and 2) to exploit the mandatory adjacency between the iris and the sclera to propose a new type of feature (*proportion of sclera*) that is fundamental in the localization of the iris, through a machine learning classification approach. Finally, a constrained polynomial fitting procedure that naturally compensates for classification inaccuracies parameterizes the pupillary and scleric iris borders.

Due to performance concerns, we aimed to preserve the linear and deterministic computational complexity of our method, offering the ability to handle real-time data. We conclude that, using a relatively small set of data for learning, our method accomplished its major goals and achieved acceptable results when compared with other state-of-the-art techniques at significantly lower computational cost.

REFERENCES

[1] Am. Nat'l Standards Inst. "American National Standard for the Safe Use of Lasers and LEDs Used in Optical Fiber Transmission Systems," ANSI Z136.2, 1988.

[2] E. Arvacheh and H. Tizhoosh, "A Study on Segmentation and Normalization for Iris Recognition," MSc dissertation, Univ. of Waterloo, 2006.

[3] A. Basit and M.Y. Javed, "Iris Localization via Intensity Gradient and Recognition through Bit Planes," *Proc. Int'l Conf. Machine Vision,* pp. 23-28, Dec. 2007.

[4] R. Battiti, "First and Second Order Methods for Learning: Between Steepest Descent and Newton's Method," *Neural Computation,* vol. 4, no. 2, pp. 141-166, 1992.

[5] N. Boddeti and V. Kumar, "Extended Depth of Field Iris Recognition with Correlation Filters," *Proc. IEEE Second Int'l Conf. Biometrics: Theory, Applications, and Systems,* pp. 1-8, Sept. 2008.

[6] C. Boyce, A. Ross, M. Monaco, L. Hornak, and X. Li, "Multispectral Iris Analysis: A Preliminary Study," *Proc. IEEE Conf. Computer Vision and Pattern Recognition Workshop Biometrics,* pp. 51-59, June 2006.

[7] R.P. Broussard, L.R. Kennell, D.L. Soldan, and R.W. Ives, "Using Artificial Neural Networks and Feature Saliency Techniques for Improved Iris Segmentation," *Proc. Int'l Joint Conf. Neural Networks,* pp. 1283-1288, Aug. 2007.

[8] Commission Int'l de l'Eclarirage, "Photobiological Safety Standards for Safety Standards for Lamps," Report of TC 6-38; CIE 134-3-99, 1999.

[9] J.G. Daugman, "Phenotypic versus Genotypic Approaches to Face Recognition," *Face Recognition: From Theory to Applications,* pp. 108-123, Springer-Verlag, 1998.

[10] J.G. Daugman, "New Methods in Iris Recognition," *IEE Trans. Systems, Man, and Cybernetics—Part B: Cybernetics,* vol. 37, no. 5, pp. 1167-1175, 2007.

[11] J. Dennis and R. Schnabel, *Numerical Methods for Unconstrained Optimization and Nonlinear Equations.* Prentice-Hall, 1983.

[12] M. Dobes, J. Martineka, D.S.Z. Dobes, and J. Pospisil, "Human Eye Localization Using the Modified Hough Transform," *Optik,* vol. 117, pp. 468-473, 2006.

[13] C. Fancourt, L. Bogoni, K. Hanna, Y. Guo, R. Wildes, N. Takahashi, and U. Jain, "Iris Recognition at a Distance," *Proc. 2005 IAPR Conf. Audio and Video Based Biometric Person Authentication,* pp. 1-13, July 2005.

[14] R. Fletcher and C. Reeves, "Function Minimization by Conjugate Gradients," *Computer J.,* vol. 7, pp. 149-154, 1964.

[15] K. Haskell and R. Hanson, "An Algorithm for Linear Least Squares Problems with Equality and Non-Negativity Constraints," *Math. Programming,* vol. 21, pp. 98-118, 1981.

[16] X. He and P. Shi, "A New Segmentation Approach for Iris Recognition Based on Hand-Heldcapture Device," *Pattern Recognition,* vol. 40, pp. 1326-1333, 2007.

[17] Y. He, J. Cui, T. Tan, and Y. Wang, "Key Techniques and Methods for Imaging Iris in Focus," *Proc. IEEE Int'l Conf. Pattern Recognition,* pp. 557-561, Aug. 2006.

[18] Z. He, T. Tan, and Z. Sun, "Iris Localization via Pulling and Pushing," *Proc. 18th Int'l Conf. Pattern Recognition,* vol. 4, pp. 366-369, Aug. 2006.

[19] Honeywell Int'l, Inc. "A Distance Iris Recognition," United States Patent 20,070,036,397, 2007.

[20] Honeywell Int'l, Inc. "Invariant Radial Iris Segmentation," United States Patent 20,070,211,924, 2007.

[21] F. Imai, "Preliminary Experiment for Spectral Reflectance Estimation of Human Iris Using a Digital Camera," technical report, Munsell Color Science Laboratories, Rochester Inst. of Technology, 2000.

[22] L.R. Kennell, R.W. Ives, and R.M. Gaunt, "Binary Morphology and Local Statistics Applied to Iris Segmentation for Recognition," *Proc. IEEE Int'l Conf. Image Processing,* pp. 293-296, Oct. 2006.

[23] X. Liu, K.W. Bowyer, and P.J. Flynn, "Experiments with an Improved Iris Segmentation Algorithm," *Proc. Fourth IEEE Workshop Automatic Identification Advanced Technologies,* pp. 118-123, Oct. 2005.

[24] C.V. Loan, "On the Method of Weighting for Equally Constrained Least Squares Problems," *SIAM J. Numerical Analysis,* vol. 22, no. 5, pp. 851-864, Oct. 1985.

[25] J.R. Matey, D. Ackerman, J. Bergen, and M. Tinker, "Iris Recognition in Less Constrained Environments," *Advances in Biometrics: Sensors, Algorithms and Systems,* pp. 107-131, Springer, Oct. 2007.

[26] P. Meredith and T. Sarna, "The Physical and Chemical Properties of Eumelanin," *Pigment Cell Research,* vol. 19, pp. 572-594, 2006.

[27] C.H. Morimoto, T.T. Santos, and A.S. Muniz, "Automatic Iris Segmentation Using Active Near Infra Red Lighting," *Proc. Brazilian Symp. Computer Graphics and Image Processing,* pp. 37-43, 2005.

[28] N.S.N.B. Puhan and X. Jiang, "Robust Eyeball Segmentation in Noisy Iris Images Using Fourier Spectral Density," *Proc. Sixth IEEE Int'l Conf. Information, Comm., and Signal Processing,* pp. 1-5, 2007.

[29] R. Narayanswamy, G. Johnson, P. Silveira, and H. Wach, "Extending the Imaging Volume for Biometric Iris Recognition," *Applied Optics,* vol. 44, no. 5, pp. 701-712, Feb. 2005.

[30] Nat'l Inst. of Standards and Technology "Iris Challenge Evaluation," http://iris.nist.gov/ICE/, 2006.

[31] B. Nemati, H. Grady Rylander III, and A.J. Welch, "Optical Properties of Conjunctiva, Sclera, and the Ciliary Body and Their Consequences for Transscleral Cyclophotocoagulation," *Applied Optics,* vol. 35, no. 19, pp. 3321-3327, July 1996.

[32] K. Park and J. Kim, "A Real-Time Focusing Algorithm for Iris Recognition Camera," *IEEE Trans. Systems, Man, and Cybernetics,* vol. 35, no. 3, pp. 441-444, Aug. 2005.

[33] P. Phillips, H. Moon, S. Rizvi, and P. Rauss, "The FERET Evaluation Methodology for Face Recognition Algorithms," *IEEE Trans. Pattern Analysis and Machine Intelligence,* vol. 22, no. 10, pp. 1090-1104, Oct. 2000.

[34] P.J. Phillips, P.J. Flynn, T. Scruggs, K.W. Bowyer, J. Chang, K. Hoffman, J. Marques, J. Min, and W. Worek, "Overview of the Face Recognition Grand Challenge," *Proc. IEEE Conf. Computer Vision and Pattern Recognition,* vol. 1, pp. 947-954, 2005.

[35] A. Poursaberi and B.N. Araabi, "Iris Recognition for Partially Occluded Images Methodology and Sensitivity Analysis," *EURASIP J. Advances in Signal Processing,* vol. 2007, pp. 20-32, Aug. 2007.

[36] M. Powell, "Restart Procedures for the Conjugate Gradient Method," *Math. Programming,* vol. 12, pp. 241-254, 1977.

[37] H. Proença and L.A. Alexandre, "Iris Segmentation Methodology for Non-Cooperative Iris Recognition," *Proc. IEE Vision, Image, & Signal Processing,* vol. 153, no. 2, pp. 199-205, 2006.

[38] H. Proença and L.A. Alexandre, "The NICE.I: Noisy Iris Challenge Evaluation, Part I," *Proc. IEEE First Int'l Conf. Biometrics: Theory, Applications, and Systems,* pp. 27-29, Sept. 2007.

[39] A. Ross, S. Crihalmeanu, L. Hornak, and S. Schuckers, "A Centralized Web-Enabled Multimodal Biometric Database," *Proc. 2004 Biometric Consortium Conf.,* Sept. 2004.

[40] A. Ross and S. Shah, "Segmenting Non-Ideal Irises Using Geodesic Active Contours," *Proc. IEEE 2006 Biometric Symp.,* pp. 1-6, 2006.

[41] S. Schuckers, N. Schmid, A. Abhyankar, V. Dorairaj, C. Boyce, and L. Hornak, "On Techniques for Angle Compensation in Nonideal Iris Recognition," *IEEE Trans. Systems, Man, and Cybernetics—Part B: Cybernetics,* vol. 37, no. 5, pp. 1176-1190, Oct. 2007.

[42] K. Smith, V.P. Pauca, A. Ross, T. Torgersen, and M. King, "Extended Evaluation of Simulated Wavefront Coding Technology in Iris Recognition," *Proc. First IEEE Int'l Conf. Biometrics: Theory, Applications, and Systems,* pp. 1-7, Sept. 2007.

[43] T. Tan, Z. He, and Z. Sun, "Efficient and Robust Segmentation of Noisy Iris Images for Non-Cooperative Segmentation," *Elsevier Image and Vision Computing J.,* special issue on the segmentation of visible wavelength iris images, to appear.

[44] M. Vatsa, R. Singh, and A. Noore, "Improving Iris Recognition Performance Using Segmentation, Quality Enhancement, Match Score Fusion, and Indexing," *IEEE Trans. Systems, Man, and Cybernetics—Part B: Cybernetics,* vol. 38, no. 4, pp. 1021-1035, Aug. 2008.

[45] P. Viola and M. Jones, "Robust Real-Time Face Detection," *Int'l J. Computer Vision,* vol. 57, no. 2, pp. 137-154, 2002.

[46] Z. Xu and P. Shi, "A Robust and Accurate Method for Pupil Features Extraction," *Proc. 18th Int'l Conf. Pattern Recognition,* vol. 1, pp. 437-440, Aug. 2006.

[47] S. Yoon, K. Bae, K. Ryoung, and P. Kim, "Pan-Tilt-Zoom Based Iris Image Capturing System for Unconstrained User Environments at a Distance," *Lecture Notes in Computer Science,* pp. 653-662, Springer, 2007.

[48] A. Zaim, "Automatic Segmentation of Iris Images for the Purpose of Identification," *Proc. IEEE Int'l Conf. Image Processing,* vol. 3, pp. 11-14, Sept. 2005.

[49] Z. Zheng, J. Yang, and L. Yang, "A Robust Method for Eye Features Extraction on Color Image," *Pattern Recognition Letters,* vol. 26, pp. 2252-2261, 2005.

[50] J. Zuo, N. Kalka, and N. Schmid, "A Robust Iris Segmentation Procedure for Unconstrained Subject Presentation," *Proc. Biometric Consortium Conf.,* pp. 1-6, 2006.

Hugo Proença received the BSc degree in mathematics/informatics from the University of Beira Interior (Portugal) in 2001. From 2002 to 2004, he was an MSc student in the artificial intelligence area at the University of Oporto (Faculty of Engineering) and received the corresponding degree in 2004. He received the PhD degree (computer science and engineering) from the University of Beira Interior in 2007. His research interests are mainly focused in the artificial intelligence, pattern recognition, and computer vision domains of knowledge, with emphasis on the biometrics area, namely the study of iris recognition systems less constrained to subjects. Currently, he serves as an assistant professor in the Department of Computer Science at the University of Beira Interior, Covilhã, Portugal, and is with the "SOCIA Lab.—Soft Computing and Image Analysis Group" and "IT—Institute of Telecommunications, Networks and Multimedia Group" research groups. He is an author/coauthor of more than 20 publications, either in ISI-indexed international journals or conferences.

▷ **For more information on this or any other computing topic, please visit our Digital Library at** www.computer.org/publications/dlib.